WFC3 Instrument Science Report 2010-04

Amplitude of fringing in WFC3/UVIS narrowband red filters

Michael H. Wong
May 18, 2010

ABSTRACT

Fringing effects in the WFC3/UVIS channel are evaluated using several methods applied to broadband-illuminated ground flat fields in all filters at wavelengths longer than 600 nm. The results from the various assessments are tabulated for each filter and can serve as rough estimates for calibration uncertainties that can impact on-orbit science data. However, differences between spectral energy distributions of on-orbit targets and of the calibration lamp can result in different fringing behavior, particularly when targets have strong spectral slopes or spectral distributions narrower than the filter bandpasses (such as emission line sources).

Histograms of fringe data can show bimodality when fringing is strong. The distance between the peaks shows that filter F953N has the greatest fringe amplitude (~16%), and that the methane quad filters FQ889N, FQ906N, FQ942N, and FQ937N have fringe amplitudes of about 10%. Manually determined fringe amplitudes in filters F656N, F658N, FQ672N, F673N, FQ674N, FQ727N, and FQ750N are lower, at 0.5–4.6%. Fringe amplitude varies over the detector surface. Filters besides the 12 listed here did not show visible signs of fringing under the continuum illumination of the calibration lamp.

Future work will provide tools for correcting fringing, after on-orbit data (calibration proposals 11922 and 12091) are obtained to test the fringe models described in Malumuth et al. (2003) and Wong (2010).

Introduction

Fringing affects UVIS data at long wavelengths because the absorption efficiency in the CCD silicon gradually decreases beyond 600–700 nm. This allows multiple internal reflections to occur between CCD detector surfaces, setting the stage for the constructive and destructive interference

that produces fringing patterns. Fringing is highly sensitive to the thickness of the silicon detector layer, so the variation of this thickness across the detector surface leads to variation in fringe amplitude, fringe phase, and quantum efficiency as a function of position on the detector. Fringing is also highly sensitive to wavelength, leading to several effects. Monochromatic illumination can produce strong fringing at long wavelengths, while broad-band illumination will average over fringe phase and produce weaker fringe patterns. For this reason, narrow-band filters show stronger fringing in the flat fields studied in this report. However, sources with narrow spectral energy distributions can produce strong fringing even if observed using a broad filter, so the results in this report apply most directly to on-orbit WFC3/UVIS observations of targets spectrally similar to the calibration lamp.

Data

Data for these tests, in the form of pipeline flat field images, were retrieved from the WFC3 calibration reference file page (http://www.stsci.edu/hst/observatory/cdbs/SIfileInfo/WFC3/reftablequeryindex) in February 2010. These flat field files are the calibration pipeline reference files, generated from stacks of individual flat field images taken during ground testing.

Statistics were compiled for subregions within each filter flat. Some filters are quad filters, in which the full UVIS detector field of view is covered by 4 filters, one for each quadrant. The filter edges are out of focus on the focal plane, so light from multiple bandpasses reaches the detector in those areas (see Fig. 6.8 in Wong et al. 2010). The filter edge effects reduce the usable area to about 1/6 of the total field of view, instead of 1/4 of the field of view. Subregions were therefore used to minimize quad filter edge effects. Although flat fields using full-frame filters are obviously not affected by quad filter edge effects, the same subsections were used in the analysis of the full-frame filter flats in order to provide consistent statistics among all the filters.

Analysis

The impact of fringing on on-orbit science data can be estimated by analyzing flat field data, but it is very important to note that sources with spectral energy distributions (SEDs) significantly different from the SED of the calibration lamp may exhibit very different behavior. In particular, although broad filters may not show fringing effects because the continuum light source smooths out wavelength-dependent fringing, these same filters can exhibit strong fringing effects when illuminated by sources with strong spectral lines or SEDs much narrower than that of the filter bandpass. Conversely, for sources with SEDs similar to the calibration lamp, fringing variability will be corrected by the flat-fielding process.

Fringe amplitudes were measured in a number of ways. Amplitudes are given as percentages of the normalized flat-field signal level. For the pixels in each subregion, the following quantities were calculated:

- rms deviation from the mean
- full width at 20% maximum
- distance between bimodal histogram peaks
- manual sampling of adjacent fringes in a single area of the detector that was most strongly affected by fringing

Statistical evaluation of the entire subregion provides the most general information on fringe amplitude in each quadrant. Both the rms deviation and the full width at 20% maximum measure the width of the pixel distribution. The rms deviation is the root-mean-square of the difference between each pixel's signal level and the mean signal level on the chip (or quadrant for quad filters). The full width at 20% maximum was calculated, instead of the full width at half maximum (FWHM), because the FWHM does not accurately characterize the width of the pixel distribution for strongly bimodal distributions (as in Figures 19 and 22). The rms deviation and the full width at 20% maximum are correlated, with the full width being about 3–3.5 times greater than the rms deviation. The ratio between these metrics depends weakly on quadrant and on fringe amplitude.

The filters with the strongest fringing (F953N, FQ889N, FQ906N, FQ924N, and FQ937N) can also be characterized by the distance between bimodal peaks of their histograms. This distance was calculated in an automated way. The lesser peak was defined as the maximum point in the lower half of the histogram, and the greater peak was defined as the maximum point in the upper half of the histogram. The dividing point was simply the middle of the range spanned by the full width at 20% maximum; this dividing point is plotted as a circle in the histograms (Figures 1 to 22). For Gaussian-like distributions (see quadrants A–C in Figure 1), this metric does not produce useful results, so the distance between histogram peaks is not reported. For quadrant D, complex distributions can be created due to the strong variation in detector layer thickness; the quad D distance between histogram peaks can therefore be underestimated by this method by about a factor of two, as shown in Figures 19 and 22.

For comparison, adjacent fringes were manually sampled in the filters most affected by fringing. Fringe amplitude is variable across the detector, so manual sampling was done near the region of each quadrant most strongly affected by fringing. In full frame filters, this region is in the thinnest part of the detector, in quadrant D, near a fringe pattern known as the "happy bunny." Typically two areas of about 900 pixels each were sampled in adjacent areas of constructive and destructive interference, with the fringe amplitude characterized by the mean of the two samples and the uncertainty in the amplitude characterized by the standard deviations of each sample.

Results

The first two metrics (rms deviation from the mean and full width at 20% maximum) are good measures of low-amplitude fringing. In flat fields with no significant fringing, rms deviations are about 1–2%, and full width at 20% maximum is about 3%. Higher values can indicate significant fringing effects, although the illumination gradient in FQ508N (Figure 20) is responsible for the

anomalously high rms deviation and full width of that filter's pixel distribution. There are tradeoffs between these two measures: rms deviation is not sensitive to broad wings of the histograms (common in quadrant D), while the full width at 20% maximum tends to overstate the effect of fringing because very few pixels fall outside this width. Thus rms deviation may be more appropriate for estimating mean signal level error due to fringing, and the full width at 20% maximum might be better suited for estimating minimum or maximum exposure times for particular science applications.

The distance between bimodal peaks of the pixel histograms is like the mode of the fringe amplitude across a quadrant, if rms deviations are more like a median of the fringe amplitude. Consult the appropriate histogram plot (in Figure 19 or 22) to interpret the values listed in Table 1 for distance between histogram peaks, because several effects can interfere with the automated method used to calculate this value. Non-bimodal distributions can give spurious results, as discussed above.

Manual sampling of adjacent fringes gives the best estimate of fringe amplitude in adjacent fringes, something that cannot easily be measured based on statistics of the quadrant as a whole. Table 1 lists peak-to-trough fringe amplitude in a single region of the detector for each filter with visible fringing patterns. The drawback of this method is that it does not evaluate the entire area of the CCD; the benefit is that fringe amplitude is variable across the detector, and this method ensures that nearby adjacent fringes are accurately characterized. These values can be taken to represent an upper limit to the fringe amplitude of a source that is dithered across adjacent fringe minima and maxima. Separations between fringe minima and maxima range from about 20 to 200 pixels (about 0.8 to 8 arcseconds on the sky).

Table 1. Flat field statistical characteristics relevant to fringe amplitudes. Values are given in units of percentage of the normalized mean signal level in each chip (for full-frame filters) or in each quadrant (for quad filters). Distance between histogram peaks is omitted for filters without clear bimodal pixel histograms; manual peak-to-trough measurements are omitted for filters without visible fringe patterns. RMS deviations and full width at 20% maximum are listed for all filters and quadrants, whether affected by fringing or not.

Filter	Quadrant	rms deviation (percent)	Full width at 20% maximum (percent)	Distance between histogram peaks (percent)	Manual peak-to-trough (percent)
F600LP	A	1.0	3.6		
F600LP	B	1.0	3.3		
F600LP	C	1.5	5.0		
F600LP	D	2.0	7.2		
F606W	A	0.9	2.9		
F606W	B	1.0	3.0		
F606W	C	1.2	3.3		
F606W	D	1.2	3.3		
F621M	A	1.0	3.3		
F621M	B	1.1	3.6		
F621M	C	1.3	3.6		
F621M	D	1.4	4.0		
F625W	A	0.9	3.0		
F625W	B	1.0	3.1		
F625W	C	1.2	3.6		
F625W	D	1.3	3.6		

Filter	Quadrant	rms deviation (percent)	Full width at 20% maximum (percent)	Distance between histogram peaks (percent)	Manual peak-to-trough (percent)
F631N	A	1.0	3.4		
F631N	B	1.3	4.2		
F631N	C	1.3	3.9		
F631N	D	1.5	4.6		
F645N	A	1.0	3.3		
F645N	B	1.3	4.6		
F645N	C	1.3	4.0		
F645N	D	1.7	5.5		
F656N	A	1.4	4.9		
F656N	B	1.3	4.5		
F656N	C	1.6	5.1		
F656N	D	1.5	5.1		3.2 ± 1.3
F657N	A	0.9	3.1		
F657N	B	1.0	3.3		
F657N	C	1.2	3.5		
F657N	D	1.3	3.7		
F658N	A	1.3	4.4		
F658N	B	1.2	3.9		
F658N	C	1.4	4.4		
F658N	D	1.3	3.7		0.9 ± 1.1
F665N	A	0.9	3.1		
F665N	B	1.1	3.4		
F665N	C	1.3	3.6		
F665N	D	1.3	4.0		
F673N	A	0.9	3.1		
F673N	B	1.0	3.2		
F673N	C	1.3	3.6		
F673N	D	1.4	4.2		0.5 ± 1.1
F680N	A	0.9	3.2		
F680N	B	1.0	3.3		
F680N	C	1.3	3.9		
F680N	D	1.5	4.7		
F689M	A	0.9	3.1		
F689M	B	1.0	3.1		
F689M	C	1.3	3.8		
F689M	D	1.4	4.2		
F763M	A	1.0	3.5		
F763M	B	1.1	3.6		
F763M	C	1.3	3.9		
F763M	D	1.8	6.1		
F775W	A	0.9	3.1		
F775W	B	1.1	3.5		
F775W	C	1.4	4.2		
F775W	D	1.8	6.3		
F814W	A	1.0	3.6		
F814W	B	1.0	3.4		
F814W	C	1.6	5.2		
F814W	D	2.3	8.3		
F845M	A	1.2	4.1		
F845M	B	1.0	3.2		
F845M	C	1.8	6.1		
F845M	D	2.4	8.4		
F850LP	A	1.3	4.5		
F850LP	B	1.1	3.7		

Filter	Quadrant	rms deviation (percent)	Full width at 20% maximum (percent)	Distance between histogram peaks (percent)	Manual peak-to-trough (percent)
F850LP	C	1.8	6.2		
F850LP	D	2.8	9.9		
F953N	A	7.6	23.7	17.8	
F953N	B	7.8	24.0	17.3	
F953N	C	7.1	23.5	14.9	
F953N	D	6.7	22.9	6.6	11.5 ± 1.6
FQ508N	A	10.5	37.9		
FQ674N	B	2.1	7.4		2.4 ± 1.3
FQ575N	C	1.4	3.8		
FQ672N	D	2.0	7.0		4.6 ± 1.3
FQ619N	A	1.5	5.5		
FQ750N	B	1.3	4.5		1.2 ± 1.1
FQ634N	C	1.4	3.9		
FQ727N	D	1.6	5.3		2.3 ± 1.1
FQ889N	A	3.8	13.5	7.8	10.0 ± 1.3
FQ906N	B	5.4	18.2	12.5	12.2 ± 1.4
FQ924N	C	4.4	16.5	6.9	10.1 ± 1.4
FQ937N	D	5.0	18.4	4.9	14.2 ± 1.4

Data images

Images of the data (subregions not affected by quadrant filter edge effects) selected to compile the statistics in Table 1 are shown here. The full WFC3 UVIS field of view is shown, with areas not used for statistics blacked out, *i.e.*, each rectangular subregion used represents about half of the full pixel area of its quadrant. The data are flat fields, with standard pipeline normalization: in full-frame flats, both chips are normalized to a 100 x 100 droplet-free and relatively flat area in quadrant A (Sabbi et al., 2009). Quad flats are similarly normalized to a 100 x 100 area within each quad. In each image, the scale ranges from 0.85 (black) to 1.10 (white), shown with a square root stretch to emphasize midrange detail.

Histograms of pixels in each quadrant are also shown. Squares indicate automatically-identified bimodal histogram peaks. These are useful only for the few cases with strongly bimodal histograms (Figures 19 and 22). The distance between these peaks is a good indicator of fringe amplitude averaged over the detector quadrant. The figures show that this metric is useful only for the filters with the strongest fringing: F953N, FQ889N, FQ906N, FQ924N, and FQ937N.

RMS deviation from the mean (error bars with triangles) and full width at 20% maximum (error bars with circles) are more useful for weaker fringe amplitudes. However, some of the variability implied by these metrics is due to other sources that are typically well-corrected by the flat-fielding stage of the standard calibration pipeline. Examples of non-fringe-related spatial signal level variation are quantum efficiency variation due to detector thickness variability (particularly in quadrant D of long-wavelength broad filters, *e.g.*, Figures 1 and 18), and filter throughput variability (*e.g.*, filter FQ508N in Figure 20).

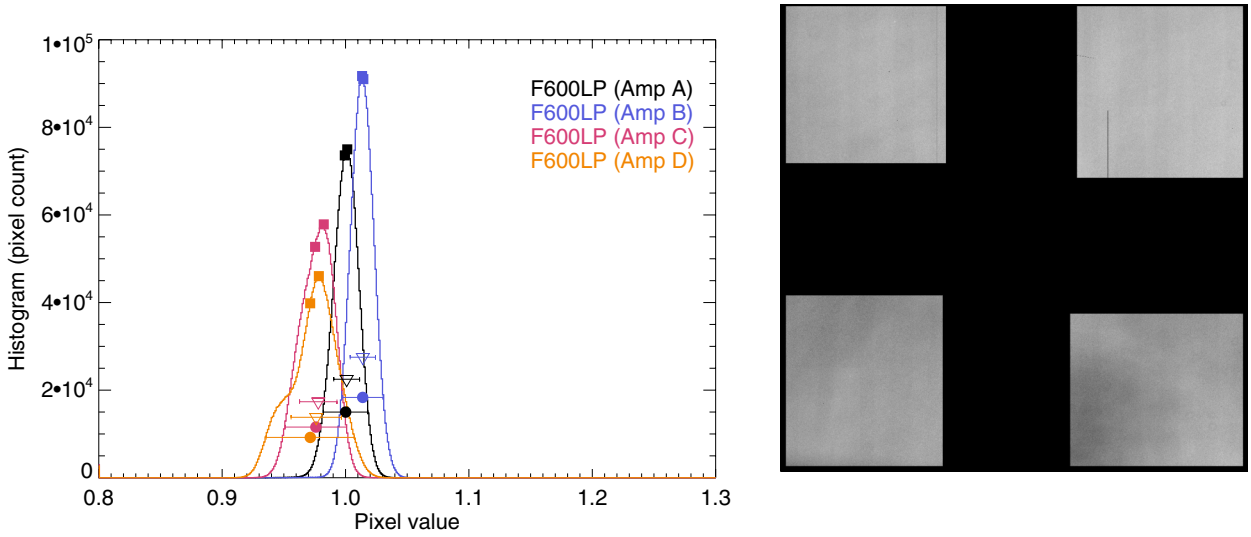

Figure 1. Histograms (left) and image (right) of the F600LP flat field. Fringe amplitudes in Table 1 are estimated based on histogram features shown here: rms deviation from the mean (error bars with triangles), full width at 20% maximum (error bars with circles), and automatically determined distance between bimodal histogram peaks (squares). Histograms are plotted separately for each amplifier subregion shown in the image. Quadrants A, B, C, and D are located respectively at upper left, upper right, lower left, and lower right.

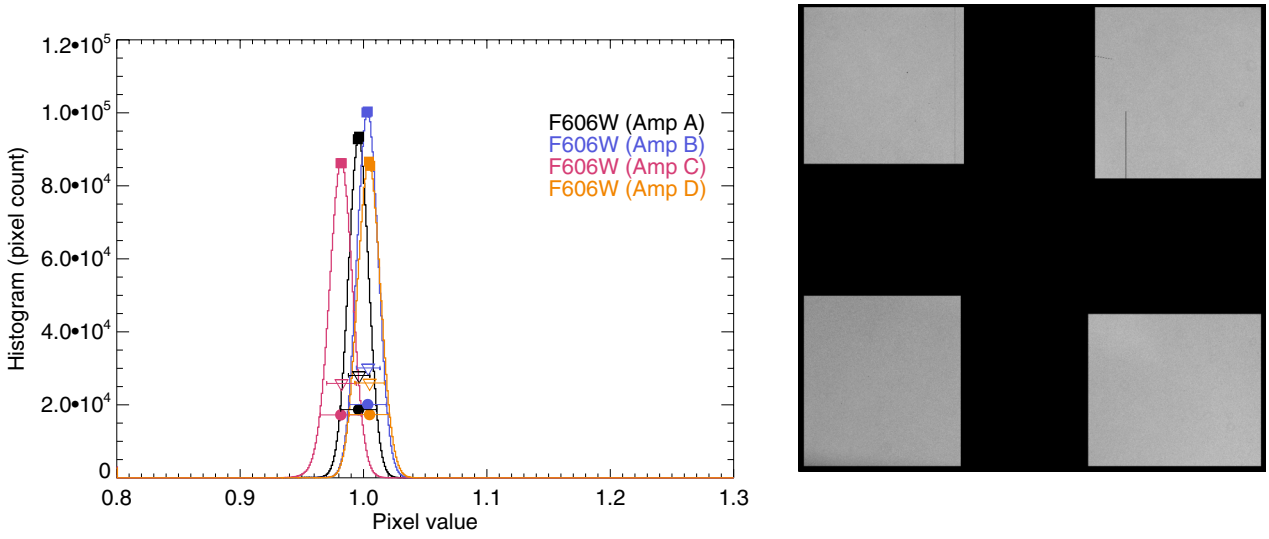

Figure 2. As Figure 1, but for the F606W flat field.

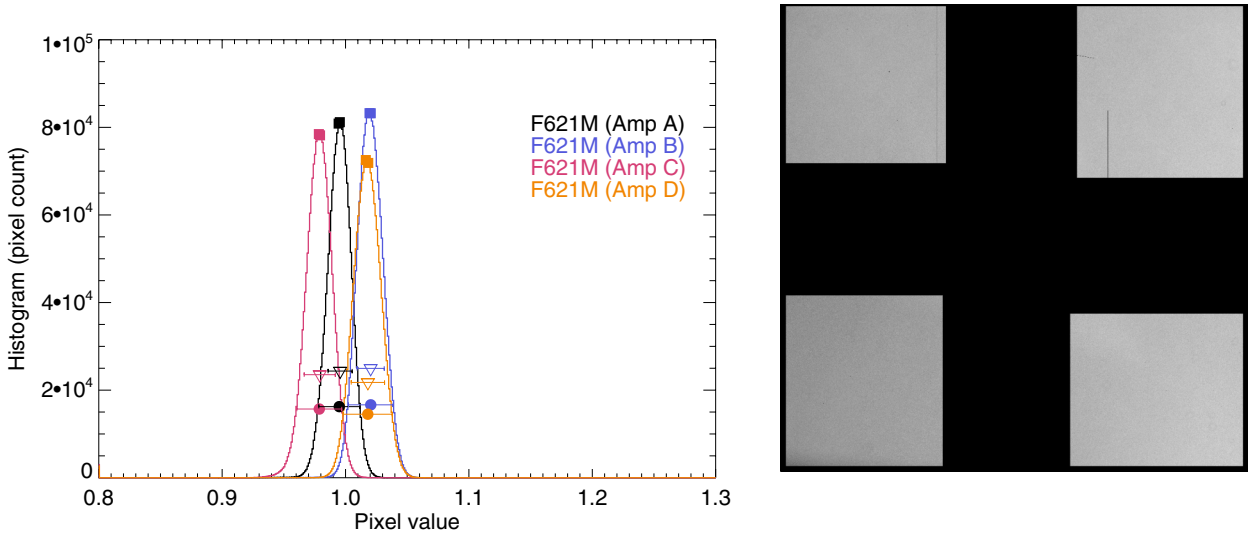

Figure 3. As Figure 1, but for the F621M flat field.

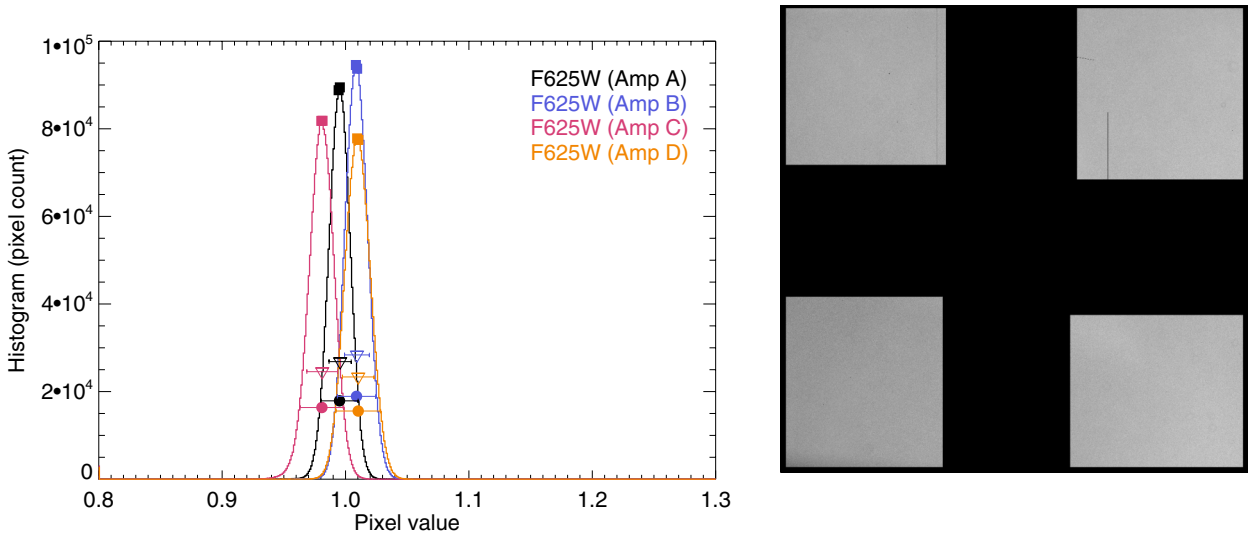

Figure 4. As Figure 1, but for the F625W flat field.

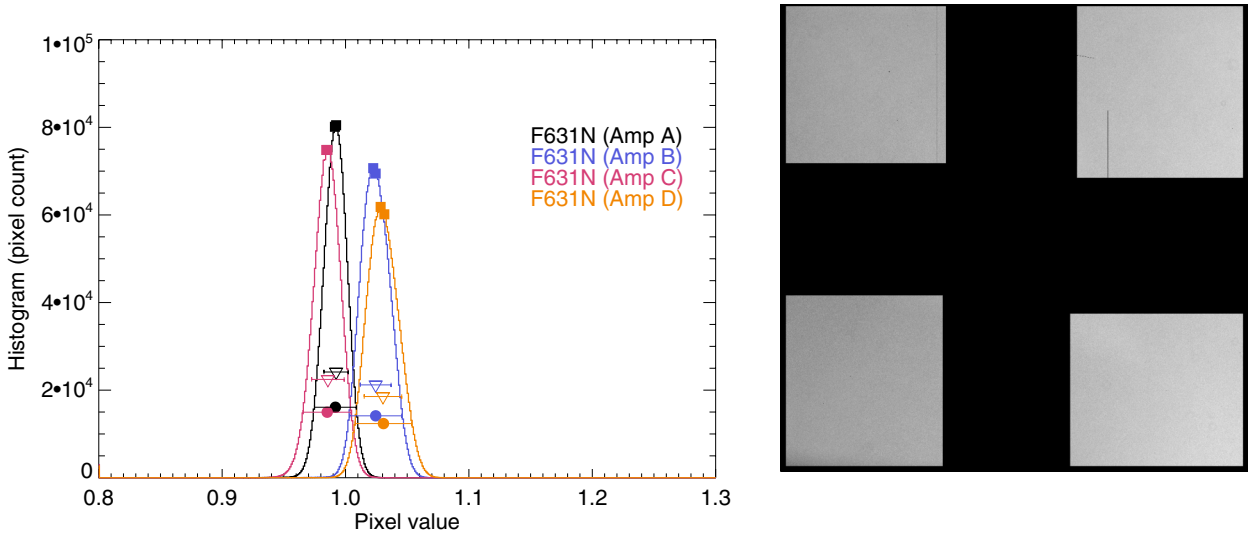

Figure 5. As Figure 1, but for the F631N flat field.

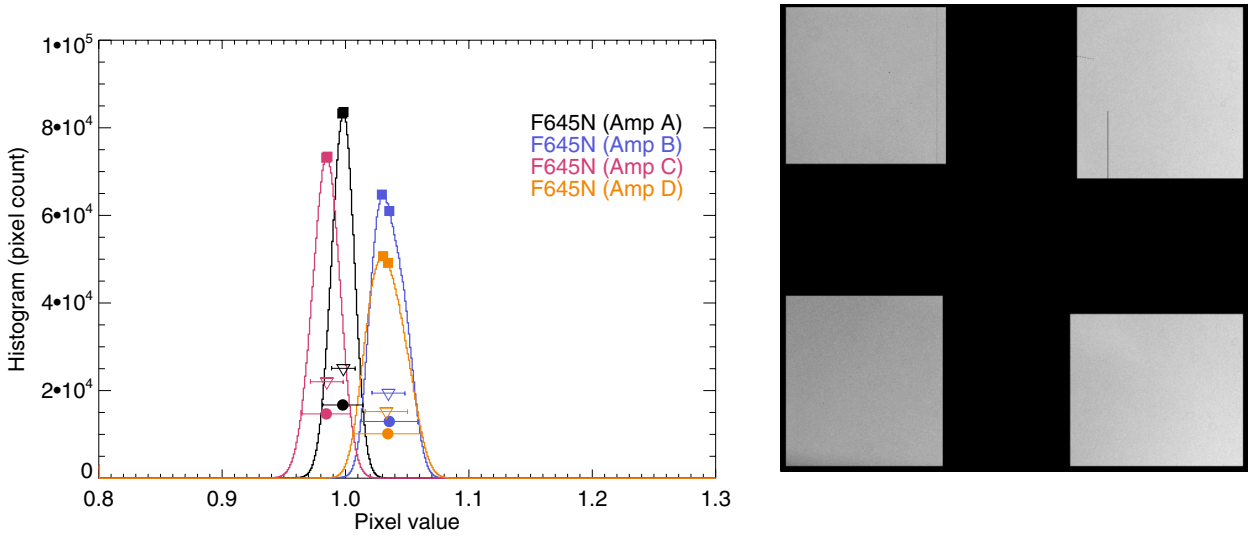

Figure 6. As Figure 1, but for the F645N flat field.

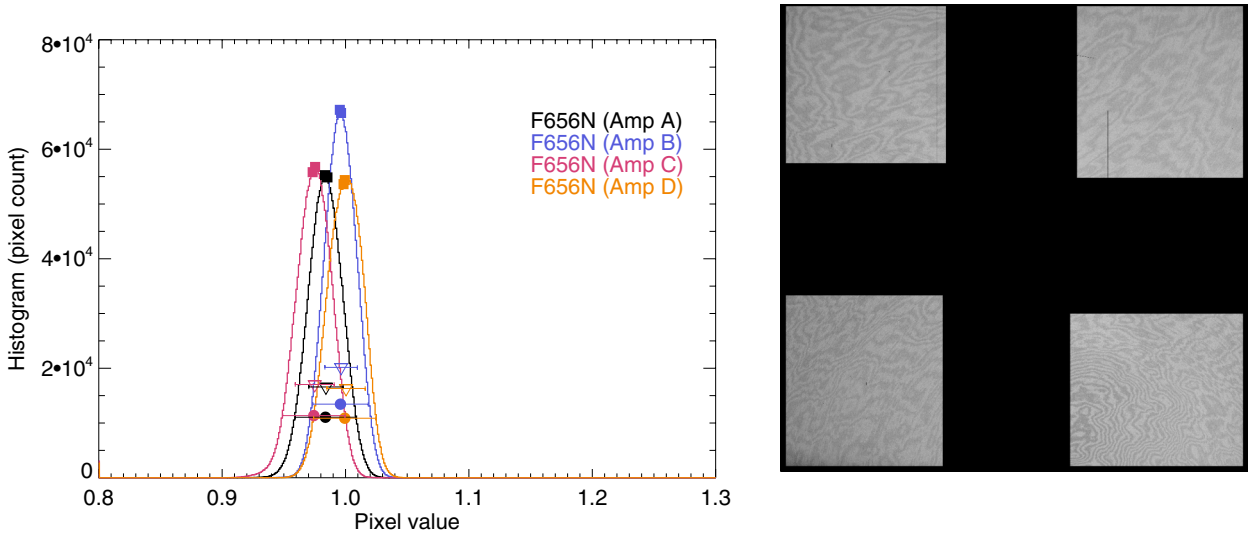

Figure 7. As Figure 1, but for the F656N flat field.

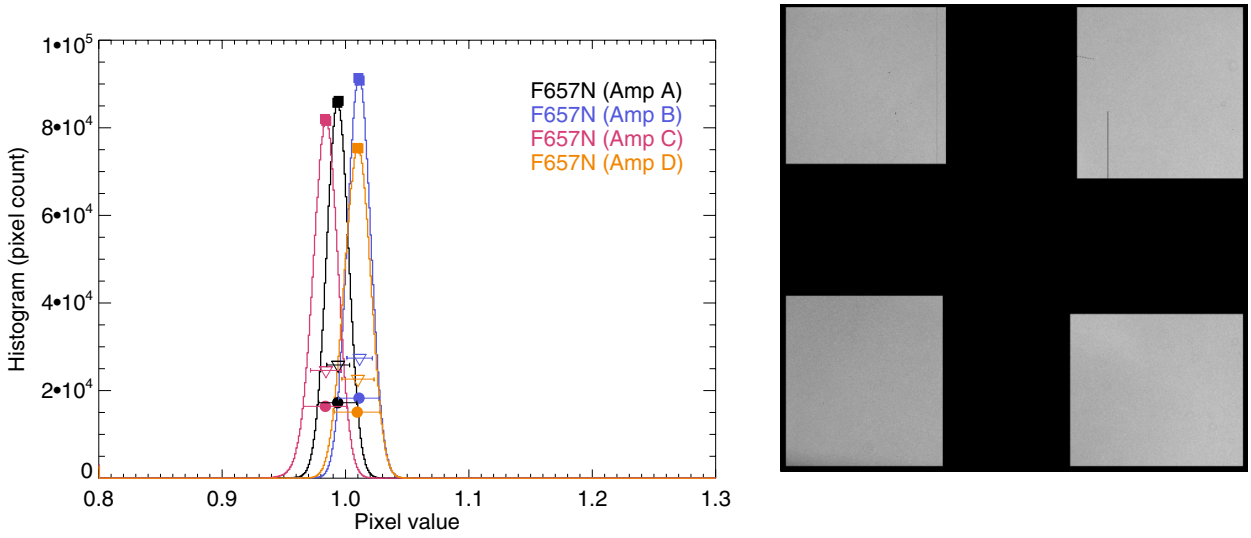

Figure 8. As Figure 1, but for the F657N flat field.

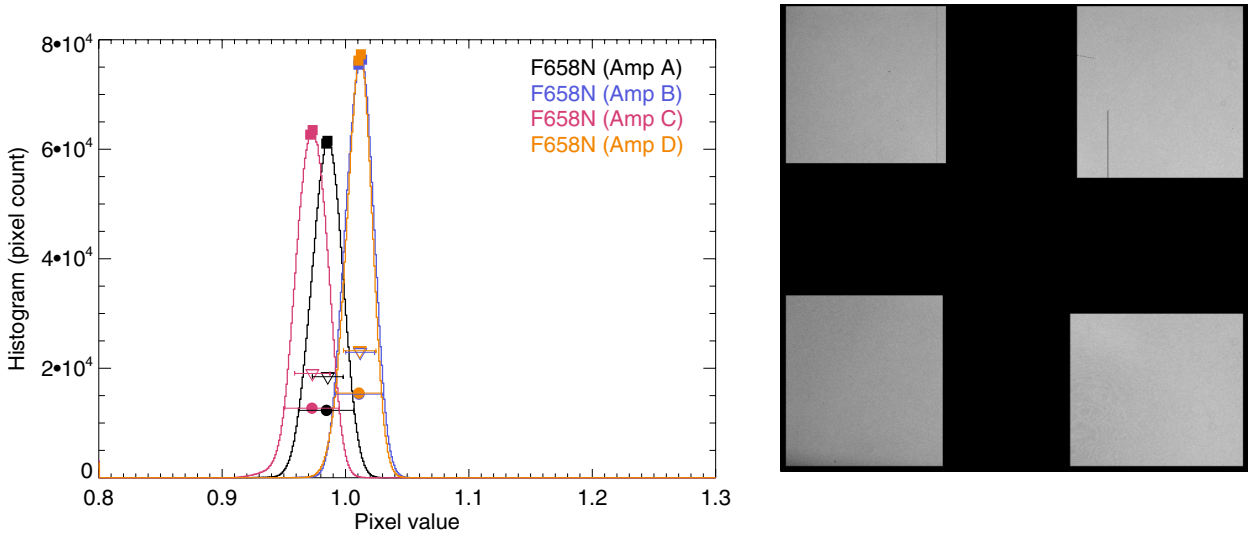

Figure 9. As Figure 1, but for the F658N flat field.

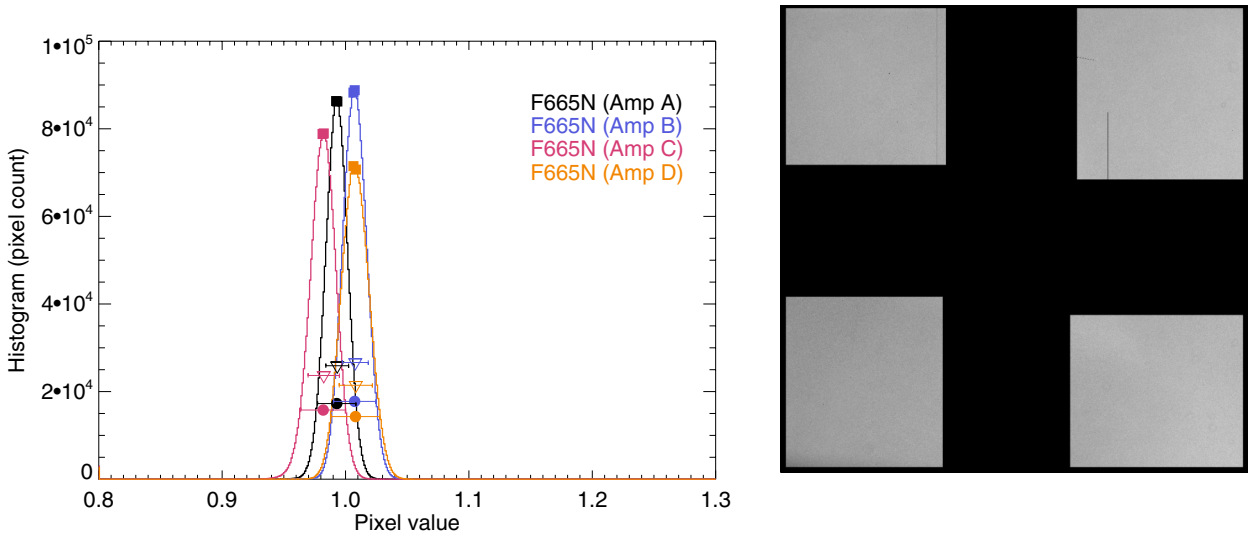

Figure 10. As Figure 1, but for the F665N flat field.

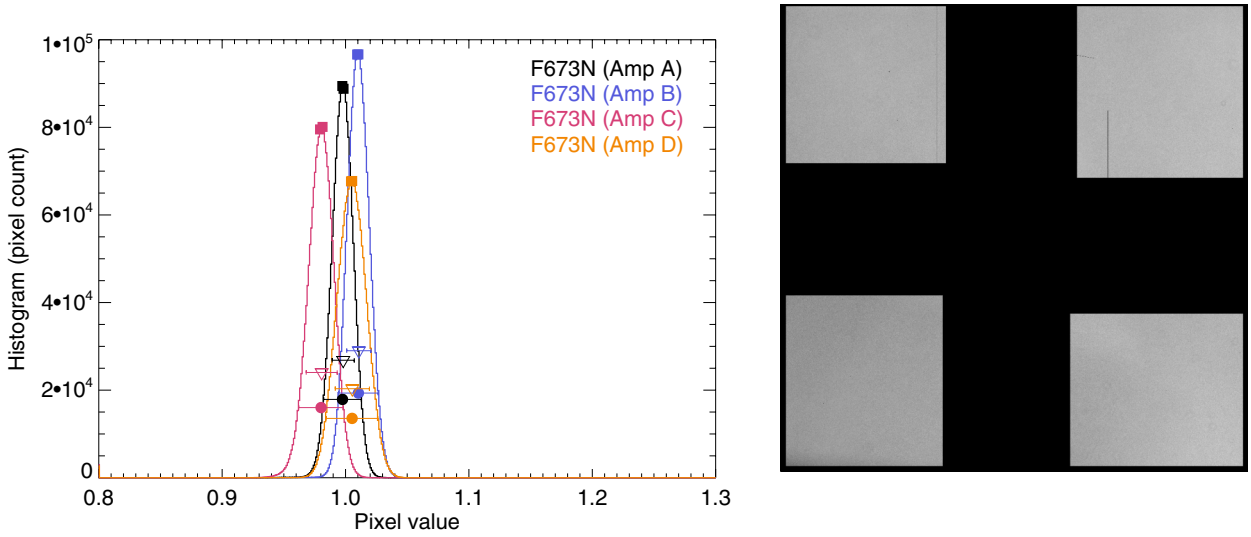

Figure 11. As Figure 1, but for the F673N flat field.

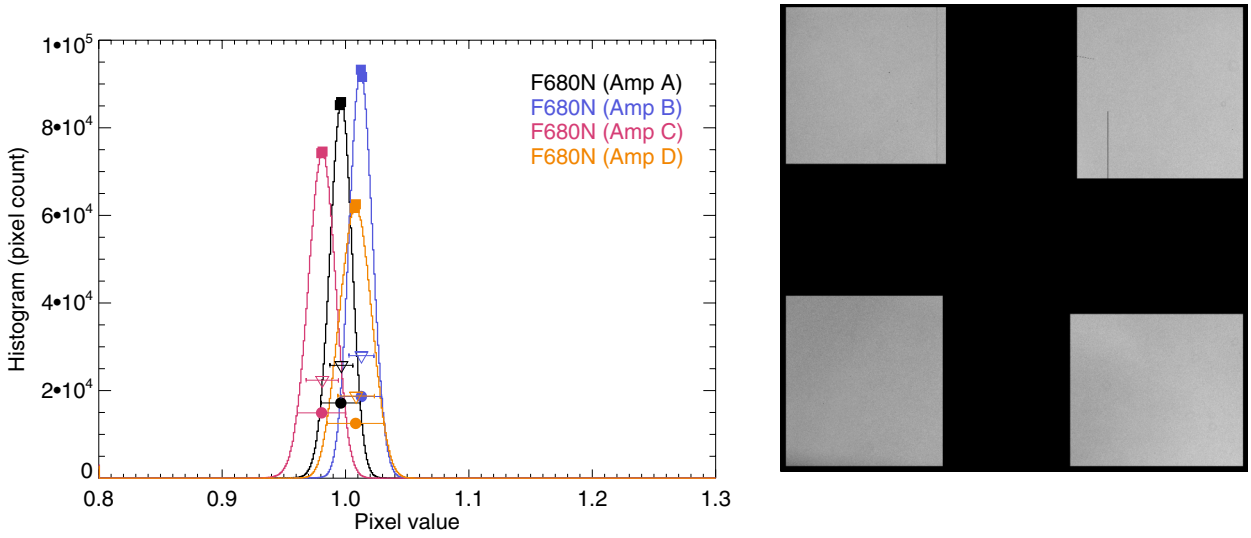

Figure 12. As Figure 1, but for the F680N flat field.

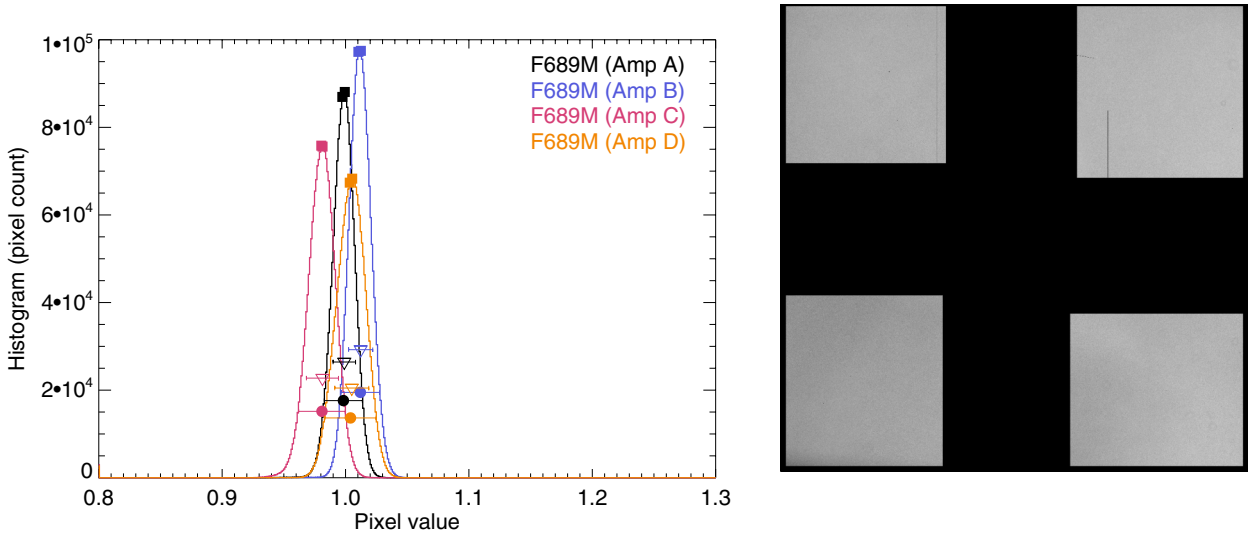

Figure 13. As Figure 1, but for the F689M flat field.

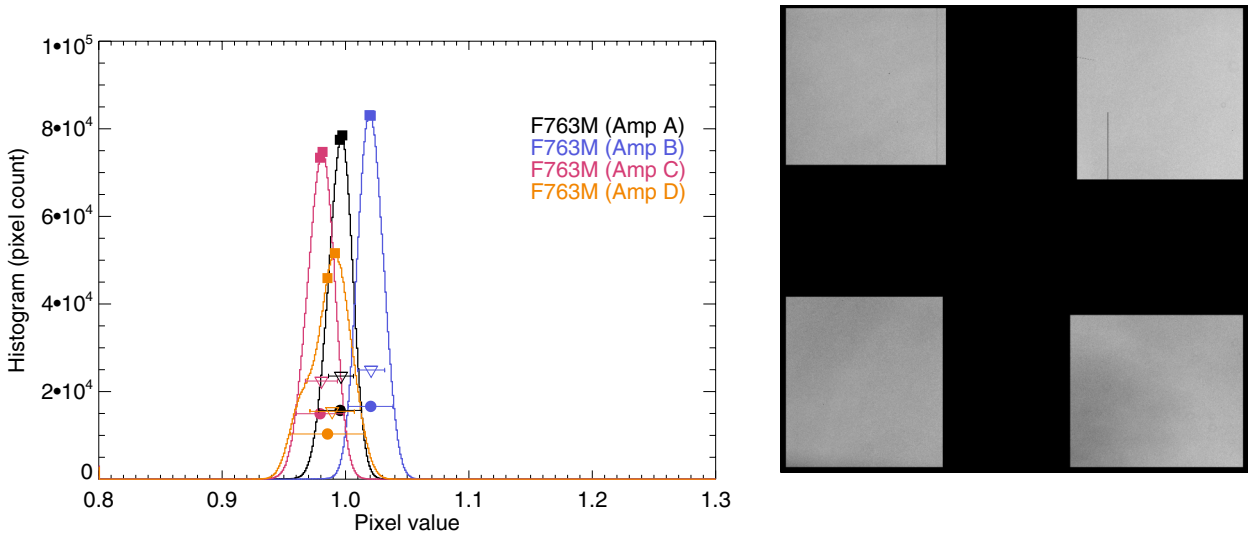

Figure 14. As Figure 1, but for the F763M flat field.

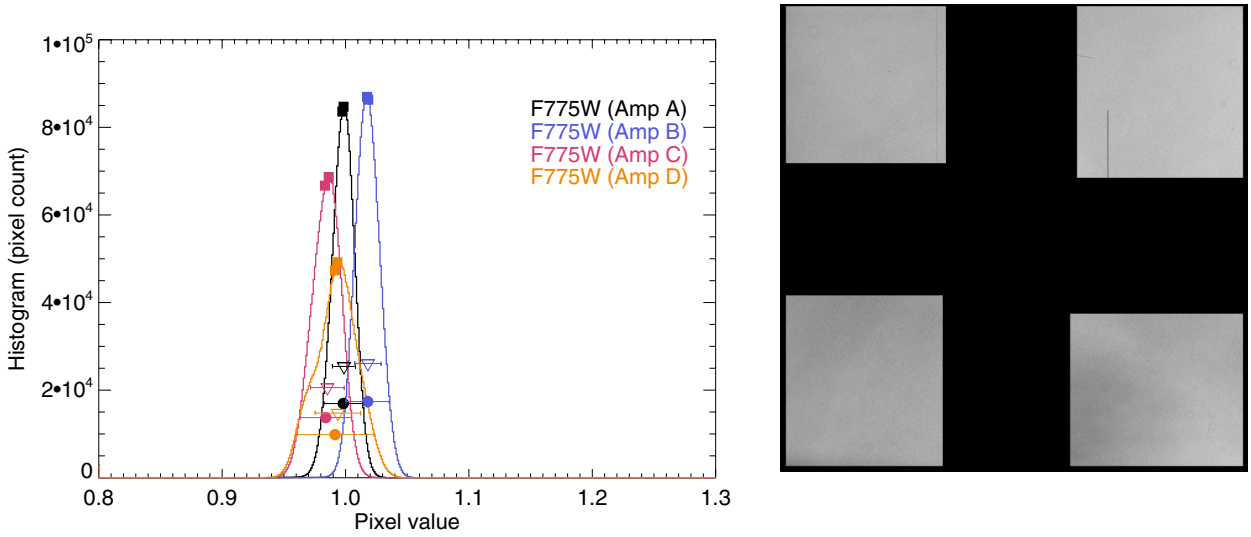

Figure 15. As Figure 1, but for the F775W flat field.

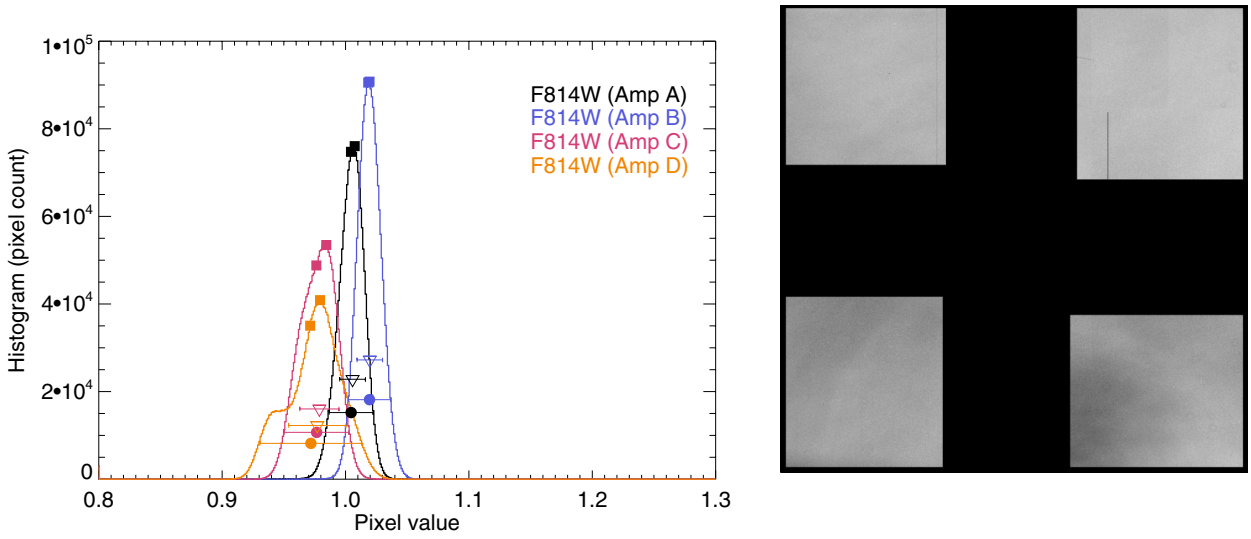

Figure 16. As Figure 1, but for the F814W flat field.

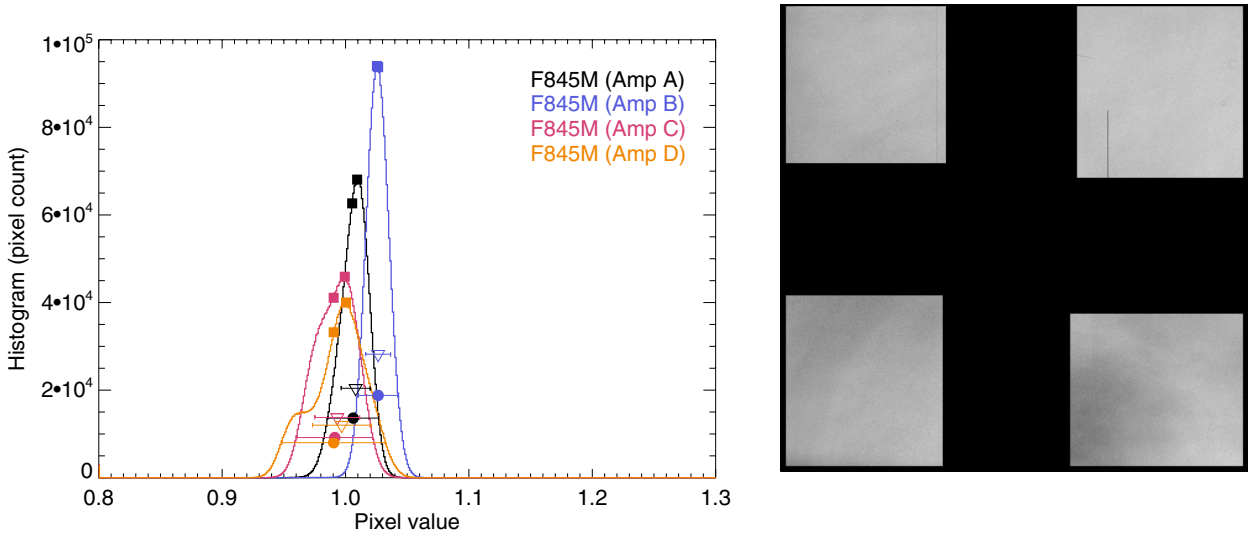

Figure 17. As Figure 1, but for the F845M flat field.

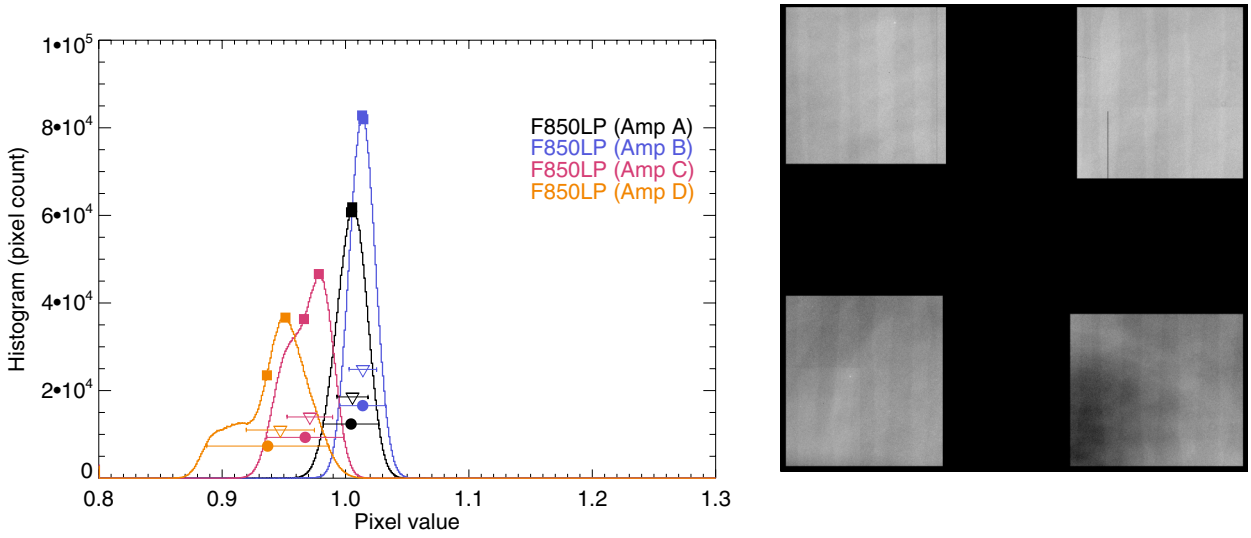

Figure 18. As Figure 1, but for the F850LP flat field.

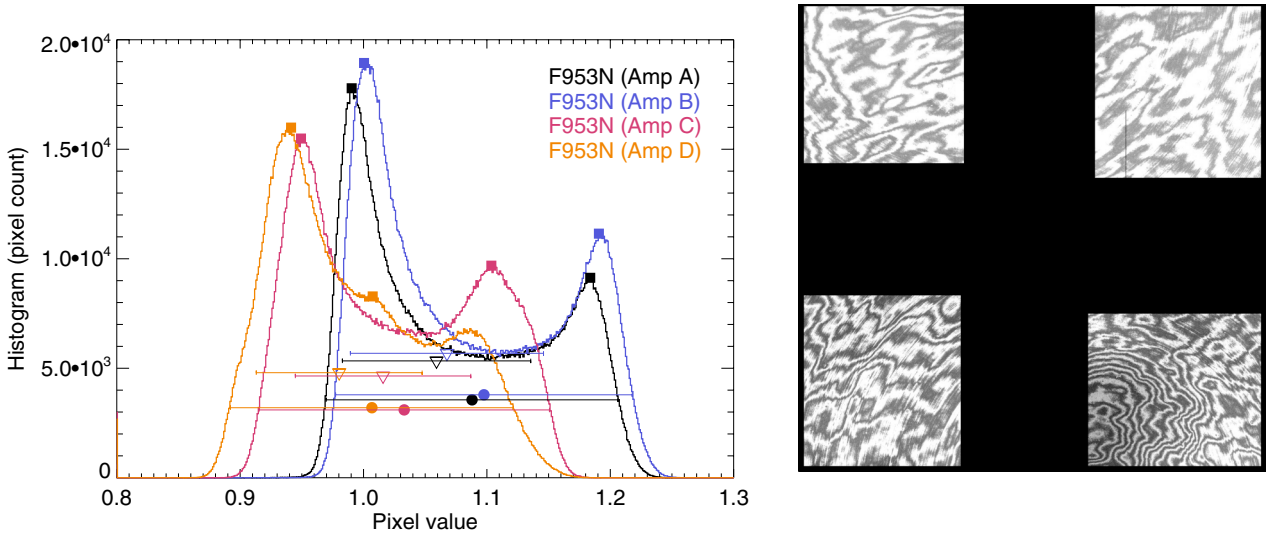

Figure 19. As Figure 1, but for the F953N flat field.

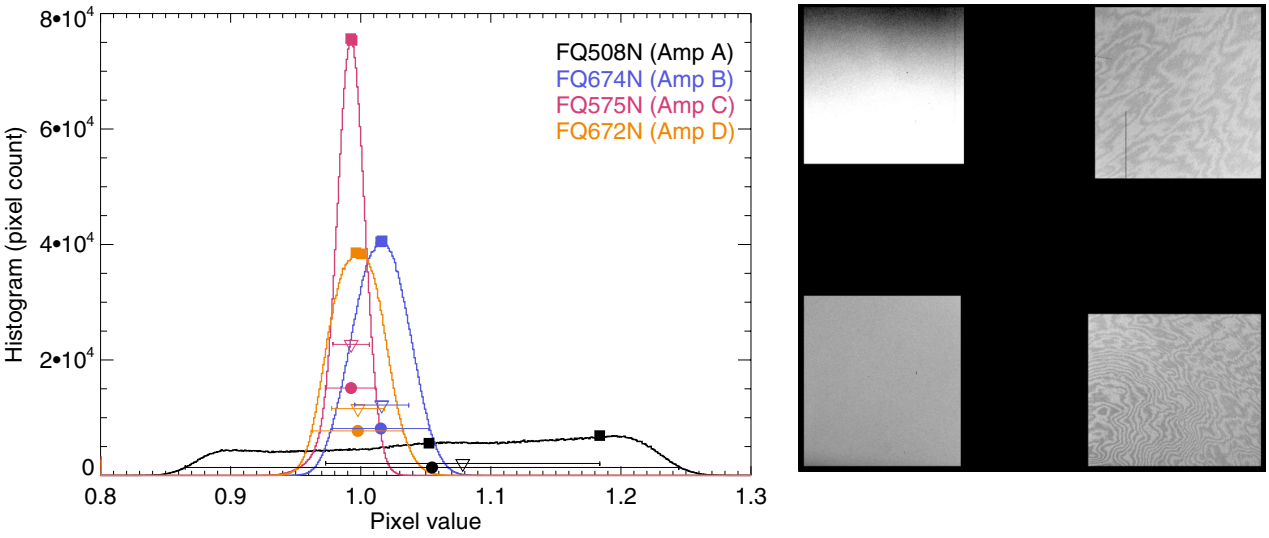

Figure 20. As Figure 1, but for the flat fields FQ508N (quadrant A, upper left), FQ674N (quadrant B, upper right), FQ575N (quandrant C, lower left), and FQ672N (quadrant D, lower right). The extremely broad distribution for FQ508N is due to a strong illumination gradient, rather than to fringing.

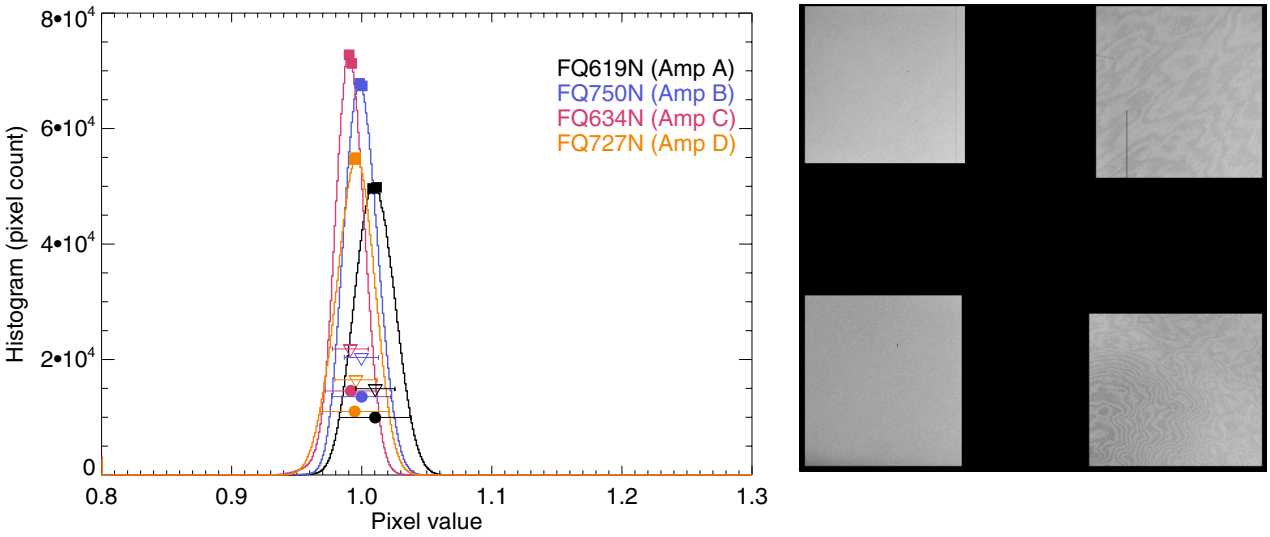

Figure 21. As Figure 1, but for the flat fields FQ619N (quadrant A, upper left), FQ750N (quadrant B, upper right), FQ634N (quandrant C, lower left), and FQ727N (quadrant D, lower right).

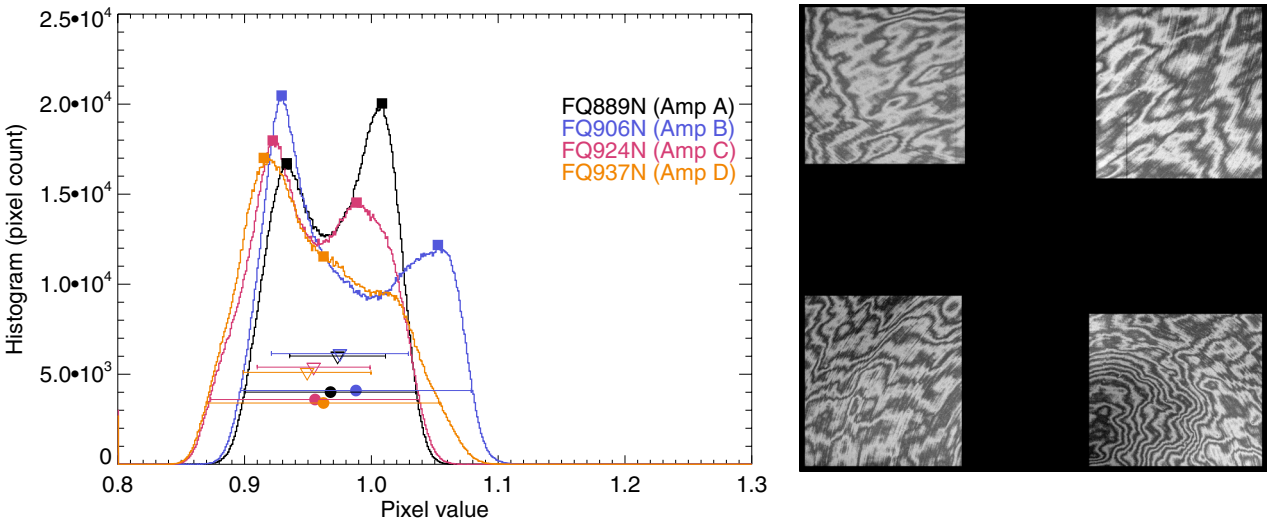

Figure 22. As Figure 1, but for the flat fields FQ889N (quadrant A, upper left), FQ906N (quadrant B, upper right), FQ924N (quandrant C, lower left), and FQ937N (quadrant D, lower right).

Conclusion

Several different methods are used to measure fringing effects in the ground test data, and the results have been tabulated as a function of filter. Observers can use one or more to crudely estimate the impact fringing is likely to have on their science data or on desired exposure times. The filter with the strongest fringing is F953N, with typical fringe amplitudes of about 16% peak to trough (determined from histogram peaks in the bimodal distribution of signal levels). The methane quad filters FQ889N, FQ906N, FQ942N, and FQ937N are also strongly affected with

typical fringe amplitudes of about 10% (again based on the bimodal histogram of pixel signal levels). Manual identification of fringing in the data show that F656N, F658N, FQ672N, F673N, FQ674N, FQ727N, and FQ750N are more weakly affected, with fringe amplitudes in the range of 0.5–4.6%.

Measurements of fringing effects in this report are only a rough guideline to the impact of fringing on actual science data, since fringing effects will be different for sources with SEDs significantly different from the calibration lamp used to create these flat fields.

Tools for correcting fringing are under development, and will be characterized with on-orbit cluster photometry. The flat fields analyzed here could serve as an additional set of test data for assessing the effectiveness of various fringe model solutions.

Acknowledgments

This work was performed while the author was a Visiting Scientist at STScI, February 2009 to 2010. Sincere thanks go to the WFC3 team (led by John MacKenty) for their support and friendliness during the visit. Eliot Malumuth, Elena Sabbi, and Jason Kalirai engaged in stimulating discussions about fringing, and Sylvia Baggett provided a thorough and helpful review of this report.

References

Malumuth, E.M., Hill, R.J., Cheng, E.S., Cottingham, D.A., Wen, Y., Johnson, S.D., Hill, R.S., 2003. Model of fringing in the WFC3 CCDs. In *Future EUV/UV and Visible Space Astrophysics Missions and Instrumentation*, J. Chris Blades, Oswald H. W. Siegmund, Editors, Proceedings of SPIE Vol. 4854.

Sabbi, E., Dulude, M., Martel, A.R., Baggett, S., and Bushouse, H., 2009. WFC3 ISR 2008-46, WFC3 UVIS ground P-flats. http://www.stsci.edu/hst/wfc3/documents/ISRs/WFC3-2008-46.pdf

Wong, M.H., 2010. WFC3 TIR 2010-01, WFC3/UVIS Fringing: Ground test data and analysis codes. Available by request from help@stsci.edu.

Wong, M.H., Pavlovsky, C., and Long, K. et al., 2010. “Wide Field Camera 3 Instrument Handbook, Version 2.0” (Baltimore: STScI)